Computers and Geotechnics 150 (2022) 104923

Contents lists available at ScienceDirect

Computers and Geotechnics

journal homepage: www.elsevier.com/locate/compgeo

Research Paper

Accurate modeling and simulation of seepage in 3D heterogeneous fractured porous media with complex structures

Luyu Wang [a,b,c,*], Yuhang Wang [a,b], Cornelis Vuik [a], Hadi Hajibeygi [b]

[a] Department of Applied Mathematics, Delft University of Technology, 2628 CD Delft, The Netherlands
[b] Department of Geoscience and Engineering, Delft University of Technology, Stevinweg 1, 2628 CV, Delft, The Netherlands
[c] GeoRessources Lab., UMR 7359, CNRS, 54500 Vandœuvre-lès-Nancy, France

ARTICLE INFO

Keywords:
Fractured porous media
Three-dimensional modeling
Seepage
Discrete fractures
Inclusions
Heterogeneity

ABSTRACT

The past decades have witnessed an increasing interest in numerical simulation for flow in fractured porous media. To date, most studies have focused on 2D or pseudo-3D computational models, where the impact of 3D complex structures on seepage has not been fully addressed. This work presents a method for modeling seepage in 3D heterogeneous porous media. The complex structures, typically the stochastic discrete fractures and inclusions, are able to be simulated. A mesh strategy is proposed to discretize the complex domain. In particular, a treatment on the intersected elements is developed to ensure a conforming mesh. Then, numerical discretization is provided, in which the flux interactions of fractures, inclusions and surrounding rock matrix are included. Numerical tests are performed to analyze the hydraulic characteristics of 3D fractured media. First, the developed framework is validated by comparing numerical solutions with the results of embedded discrete fracture model. Next, the effects of orientation, aperture and radius of fractures on fluid flow and equivalent permeability tensor are analyzed. The variations of pressure distribution are studied in heterogeneous and homogeneous media. Finally, the hydraulic properties of a medium with complex structures are investigated to show the difference of hydraulic feature between fractures and inclusions.

1. Introduction

Modeling of seepage in fractured porous media is of great interest in geotechnical engineering and geoscience applications (Hajibeygi et al., 2020; Mejia et al., 2021; Wang et al., 2022a). In practice, fractures are randomly distributed in the geological fields, and they have contrasting hydraulic properties compared to that of the rock matrix (Berkowitz, 2002; Kolditz et al., 2012; Adler et al., 2013). As a result, fractures play a critical role in determining the dynamics of flow and transport in such fractured systems.

There are different approaches for numerical investigation of fractured porous media. They can be mainly divided into two categories. The first category is related to the geological modeling techniques and thegeostatistics (Yin and Chen, 2020; Jacquemyn et al., 2021; Cañamón et al., 2022), which also studies the distribution law of natural fractures from the perspective of the statistical methods. In this category, field investigation provides the massive data of geological information of fractures. The researchers do not focus on numerical simulations, such as the seepage and deformation simulations, but study the statistical characteristics of fracture networks. However, the second category focuses on the numerical methods related to hydraulic and mechanical processes of the deformable fractured media, in which the finite element method and the finite volume method are the commonly used numerical approaches (Karimi-Fard and Durlofsky, 2012; Wang et al., 2020, 2022b; Hajibeygi et al., 2020; Sui et al., 2022). In the presented study, we mainly focus on the second category.

Three representative numerical models have been widely used to simulate seepage in fractured porous media, namely, (a) the equivalent continuum model (ECM) (Ghahfarokhi, 2017; Chung et al., 2018; Wang et al., 2022a), (b) the discrete fracture network (DFN) (de Dreuzy et al., 2013; Hyman et al., 2015), and (c) the discrete fracture model (DFM) (Karimi-Fard et al., 2004; Zidane and Firoozabadi, 2018; Wang et al., 2022c). The ECM, which is proposed based on the upscaling technique, is an efficient computational model but it cannot reflect the interaction between the fractures and the rock matrix. Especially, for a fractured medium with a few fractures with large size, the equivalent permeability tensor may not exit. In this case, the ECM does not work. The DFN is a simplified model which neglects flow in the rock matrix. It provides an acceptable solution if the permeability of fractures is

* Corresponding author.
E-mail addresses: wang.luyu@cnrs.fr, luyu.wang@hotmail.com (L. Wang), y.wang-25@tudelft.nl (Y. Wang), c.vuik@tudelft.nl (C. Vuik), h.hajibeygi@tudelft.nl (H. Hajibeygi).

https://doi.org/10.1016/j.compgeo.2022.104923
Received 18 February 2022; Received in revised form 21 June 2022; Accepted 10 July 2022
Available online 22 July 2022
0266-352X/© 2022 The Author(s). Published by Elsevier Ltd. This is an open access article under the CC BY-NC-ND license (http://creativecommons.org/licenses/by-nc-nd/4.0/).

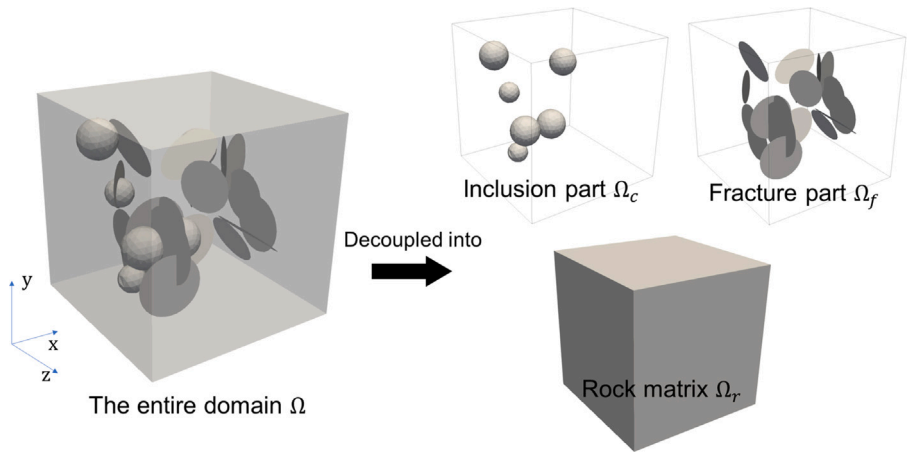

Fig. 1. Schematic of a 3D porous medium with discrete fractures and inclusions.

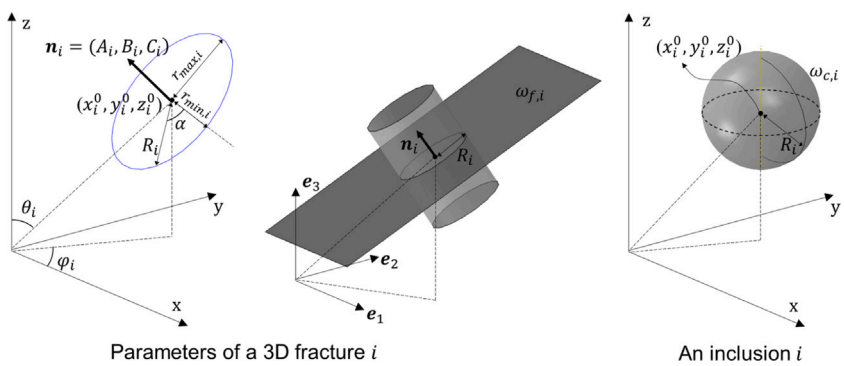

Fig. 2. Parameters of a 3D fracture and an inclusion.

much higher than that of the rock matrix, whereas the validity will be violated if fracture permeability is comparable or even lower compared to the matrix. Therefore, in the past decades, the DFM was proposed to accurately simulate seepage in fractured reservoirs. In contrast to ECM and DFN, it accounts for the flux exchange between the matrix and the lower-dimensional discrete fractures. It models the control volumes associated with the intersected fractures through a star-delta transformation, as described by Karimi-Fard et al. (2004). As such, DFM enabled simulation of multiphase flow in porous reservoirs with multiple intersecting fractures. The advantages of DFM, through its accurate transmissibility calculations and complex conforming mesh requirements, come with the major challenge of extending it to 3D domains with complex fracture geometries (Hyman et al., 2014; Karimi-Fard and Durlofsky, 2016; Huang et al., 2021).

Several simplifications have been introduced to overcome with the DFM challenges associated with unstructured complex mesh in 3D domains. Examples include the boundary element method (Dershowitz and Fidelibus, 1999) and the pipe-network method (Cacas et al., 1990). The basic principle of these methods is to reduce the 3D problem to 2D problem, to achieve the efficient simulations. Nevertheless, these treatments fall short of describing the complex structures, such as the discrete fractures and inclusions. To achieve the flux connection between the fractures and the surrounding matrix, the conforming scheme based on the unstructured grids has been employed to discretize such geometries (Hyman et al., 2015; Wang and Shahvali, 2016; Zidane and Firoozabadi, 2018). Normally, the rock matrix is discretized by the tetrahedrons, while the fractures are discretized by the triangles. To this end, the conforming Delaunay algorithm has been developed for 3D discrete fractures (Hyman et al., 2014; Karimi-Fard and Durlofsky, 2016). In addition, the commonly used two-point flux approximation scheme requires k-orthogonal grids in the case of anisotropic permeability fields, which can impose limitations for real-field applications. To resolve this issue, the grid optimization technique has been presented to improve the grid orthogonality (Karimi-Fard, 2008; Karimi-Fard and Durlofsky, 2012). Furthermore, a novel meshing strategy has been devised to generate an unstructured system with high quality grids for both the matrix and 3D fractures (Karimi-Fard and Durlofsky, 2016).

Modeling approaches for 2D fractured porous media have been well developed over the past decades, where fractures are directly depicted by line segments (Hajibeygi et al., 2011; Tan et al., 2021; Wang et al., 2022c). In 3D space, however, fractures are represented by planes or surfaces, in which numerical treatment on intersected fractures still remains a challenge (de Dreuzy et al., 2013; Hyman et al., 2015; Huang et al., 2021). Moreover, in geological fields, the coexistence of the discrete fractures and inclusions (Wang et al., 2022a), adds to the difficulty of partitioning the computational domain, which has become one of the key challenges in numerical simulations. At present, commercial software cannot even fully addressed these challenges (Kolditz et al., 2012; Zidane and Firoozabadi, 2018; Bilke et al., 2019). Therefore, it is critical to develop an efficient and robust modeling and meshing strategy that is able to capture the complex topological structures in 3D domain (Hyman et al., 2014; Huang et al., 2021). To the best of our knowledge, this task has not been fully resolved. There is a common treatment that 3D fractures are modeled as pseudo-3D geometries, which are created directly by stretching the 2D planar fractures (Ahmed et al., 2015; Yan et al., 2018). Obviously, this treatment is oversimplified and fails to reflect the geometrical complexities and the relations between the rock matrix and the 3D fractures.

Despite being crucially important, numerical simulation of the 3D fractured media with complex structures remains to a large extend unexplored. In this work, we present a 3D discrete fracture modeling

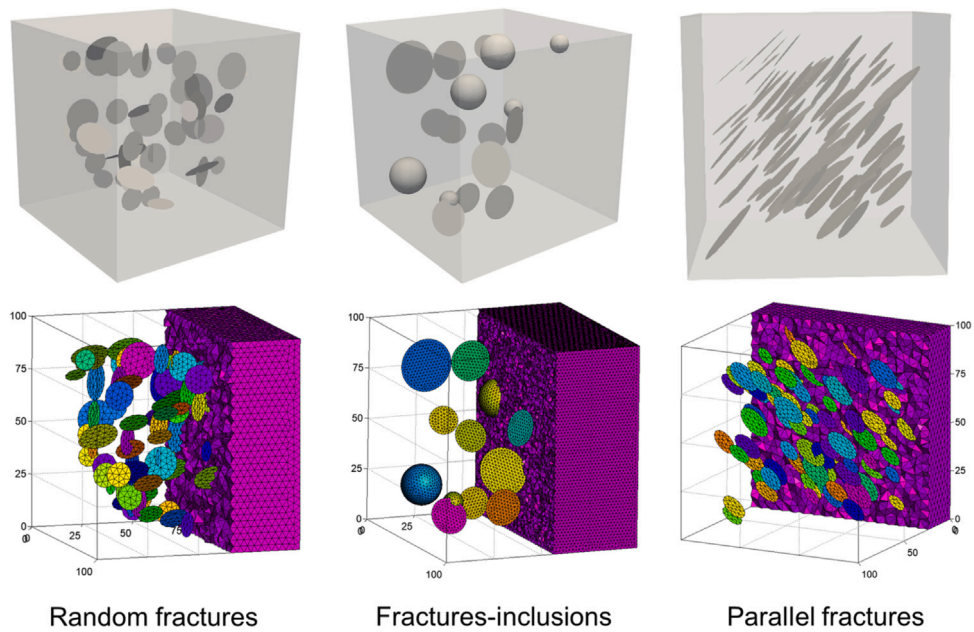

Fig. 3. Visualization (top row) and mesh partition (bottom row) of several typical patterns.

approach which is based on the DFM concepts. The complex geometrical structures, especially the stochastic fractures and inclusions, are explicitly captured in the presented framework. Appropriate treatments for the conforming grids are presented, specially for the intersecting fractures and inclusions. Then, using the developed DFM strategy, the effect of complex structures on seepage is analyzed for several test cases.

The rest of this paper is organized as follows. First, the description of 3D complex structures and the meshing strategy are provided in Section 2. Then, the governing equations of seepage are presented in Section 3. Later, numerical discretization is provided based on two-point flux approximation (TPFA). Grid convergence evaluation and numerical validation are carried out to verify the presented method. Finally, numerical tests are conducted to study the hydraulic characteristics of the 3D fractured porous media, in which the effects of heterogeneity and the complex structures are studied.

2. Modeling approach

In this section, a modeling approach based on the analytic geometry is introduced to describe the position, size and orientation of the 3D discrete fractures. Then, the discrete fractures and inclusions are generated according to the statistical laws. A meshing strategy is given based on the conforming unstructured grids.

2.1. Description of 3D fractures and inclusions

As shown in Fig. 1, we define three main components for a porous media, namely the rock bulk Ω_r, the union of all fractures Ω_f and the union of all inclusions Ω_c. The entire domain Ω consists of the union of these three components:

$$\Omega = \Omega_r \cup \Omega_f \cup \Omega_c \tag{1}$$

A strict constraint is that any overlapping among Ω_r, Ω_f and Ω_c is not allowed. Obviously, Ω_f and Ω_c can be then decomposed as:

$$\Omega_f = \cup_{i=1}^{N_f} \omega_{f,i}, \quad \Omega_c = \cup_{i=1}^{N_c} \omega_{c,i} \tag{2}$$

where N_f and N_c are the numbers of fractures and inclusions, respectively. $\omega_{f,i}$ or $\omega_{c,i}$ is an individual fracture or inclusion, as shown in Fig. 2.

The key point is to obtain the explicit expressions of $\omega_{f,i}$ and $\omega_{c,i}$ in Eq. (2). Here we provide an efficient way to represent the fractures and inclusions based on the analytic geometry.

For convenience, we use the planar assumption of a fracture. As displayed in Fig. 2, the radius R_i of an 3D elliptical fracture i along the direction α is generally given by (Swokowski, 1979; Qiu, 2017):

$$R_i = \frac{1 + \tan^2 \alpha}{(1/r_{max,i})^2 + (\tan \alpha / r_{max,i})^2} \tag{3}$$

where $r_{max,i}$ and $r_{max,i}$ are the minor and major axes of the elliptical fracture.

Then, we introduce the disk assumption of fractures (Mustapha et al., 2011; Hyman et al., 2015; Huang et al., 2021). It assumes that the shape of a fracture is a flat disk, which leads to $r_{max,i} = r_{min,i}$ in Eq. (3).

Consequently, to define a 3D fracture i, the key geometrical parameters should be given, as shown in Fig. 2, including the coordinates of center point $O_i(x_i^0, y_i^0, z_i^0)$, the radius R_i, the two azimuth angles φ_i and θ_i.

The orientation of fracture i is determined by the normal vector $\mathbf{n}_i$, which is calculated by the two azimuth angles, $\mathbf{n}_i = (A_i, B_i, C_i)$. The expressions of these components are $A_i = |\mathbf{n}_i| \sin\theta_i \cos\varphi_i$, $B_i = |\mathbf{n}_i| \sin\theta_i \sin\varphi_i$ and $C_i = |\mathbf{n}_i| \cos\theta_i$.

The plane, where the fracture i lies, is expressed by the plane equation based on the normal vector $\mathbf{n}_i$ (Swokowski, 1979; Qiu, 2017):

$$A_i x + B_i y + C_i z + D_i = 0 \tag{4}$$

where D_i is the intercept of the plane, determined by the center point and the normal vector of this fracture, $D_i = -\left(A_i x_i^0 + B_i y_i^0 + C_i z_i^0\right)$.

Therefore, we obtain the geometrical equation of the plane based on analytic geometry:

$$z = \frac{\sin\theta_i \cos\varphi_i}{\cos\theta_i}\left(x_i^0 - x\right) + \frac{\sin\theta_i \sin\varphi_i}{\cos\theta_i}\left(y_i^0 - y\right) + z_i^0 \tag{5}$$

In addition, to define the spatial range of a fracture, the boundaries should be given. Here, as show in Fig. 2, we use a cylinder to confine the range of a fracture in the plane. The equation of the cylinder reads (Swokowski, 1979; Qiu, 2017):

$$\left\| \begin{matrix} \mathbf{e}_1 & \mathbf{e}_2 & \mathbf{e}_3 \\ x - x_i^0 & y - y_i^0 & z - z_i^0 \\ A_i & B_i & C_i \end{matrix} \right\| = R_i \tag{6}$$

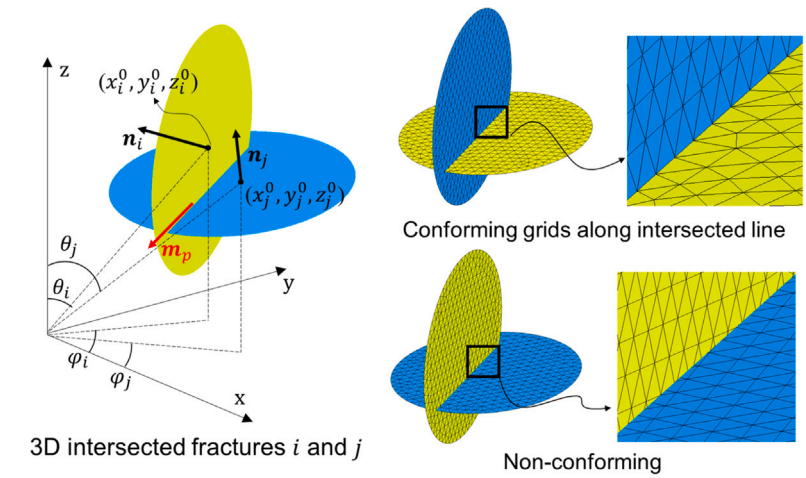

(a) Intersected fractures

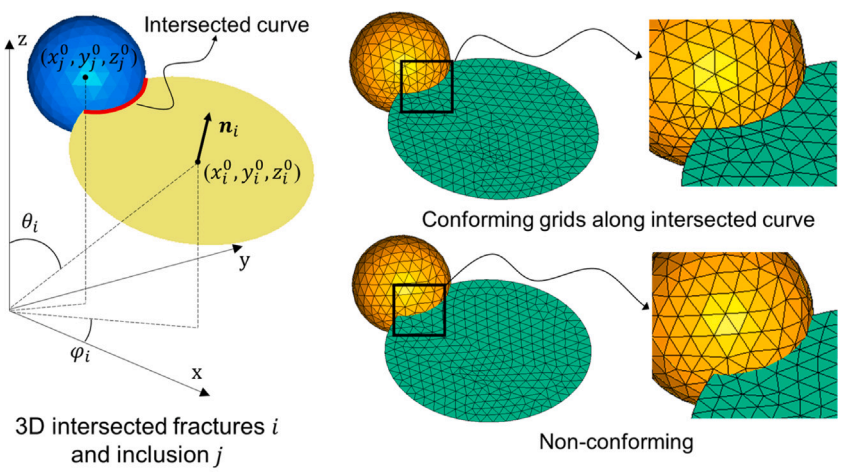

(b) Intersected fracture and inclusion

Fig. 4. Schematic of 3D intersected geometries and the arrangement of grids.

where R_i is determined by Eq. (3). $\|.\|$ is the 2-norm of matrix. $\mathbf{e}_1$, $\mathbf{e}_2$ and $\mathbf{e}_3$ are the three unit basis vectors of the global coordinate system, as shown in Fig. 2.

For the inclusions, we apply the spherical assumption. It assumes that the inclusions are spheres in 3D space. We employ the similar notations in the above fracture description. The geometrical parameters of an inclusion i include the center point of the sphere $O_i(x_i^0, y_i^0, z_i^0)$ and the radius R_i, as shown in Fig. 2. The equation of inclusion i reads:

$$\left(x - x_i^0\right)^2 + \left(y - y_i^0\right)^2 + \left(z - z_i^0\right)^2 \le R_i^2 \tag{7}$$

2.2. Fracture generation and visualization

Eqs. (5) and (6) provide the explicit expressions of a fracture, and Eq. (7) defines an inclusion. We use these expressions iteratively, until N_f and N_c, then all of the fractures and inclusions can be generated and visualized.

The key parameters are obtained by the random number generator:

$$\mathrm{Rand}(x_i^0, y_i^0, z_i^0, R_i, \varphi_i, \theta_i), \quad i = 1 \sim N_f \tag{8}$$

According to the field investigations, the distribution of stochastic fractures inside a geological domain follows the statistical laws (de Dreuzy et al., 2013; Hyman et al., 2015), typically the Fisher distribution, normal distribution and the logarithmic normal distribution. Therefore, the generator Eq. (8) obeys the statistical laws, where different parameters are allowed to be assigned to different distribution laws. We refer to literature (Hyman et al., 2016; Wu et al., 2021) for the details. Several typical examples with different patterns are displayed in Fig. 3.

2.3. Strategy of mesh partition

The unstructured grids are generated based on the Delaunay tetrahedrons and triangles (Shewchuk, 2002; Hyman et al., 2014). It follows the conforming scheme, in which the high-dimensional cells (the matrix and inclusion cells) are confined by the relative low-dimensional cells (the fracture cells).

Especially, the treatment at the intersected fractures should be drawn attention. According to the principle of conforming meshes, the matrix cells should be arranged along the intersected line between two crossing fractures. Otherwise, the overlapping between them will happen, then the correct topological relation may be broken.

To solve this issue, we build the equation of the intersected line. As shown in Fig. 4a, the two crossing fractures are labeled as i and j, then

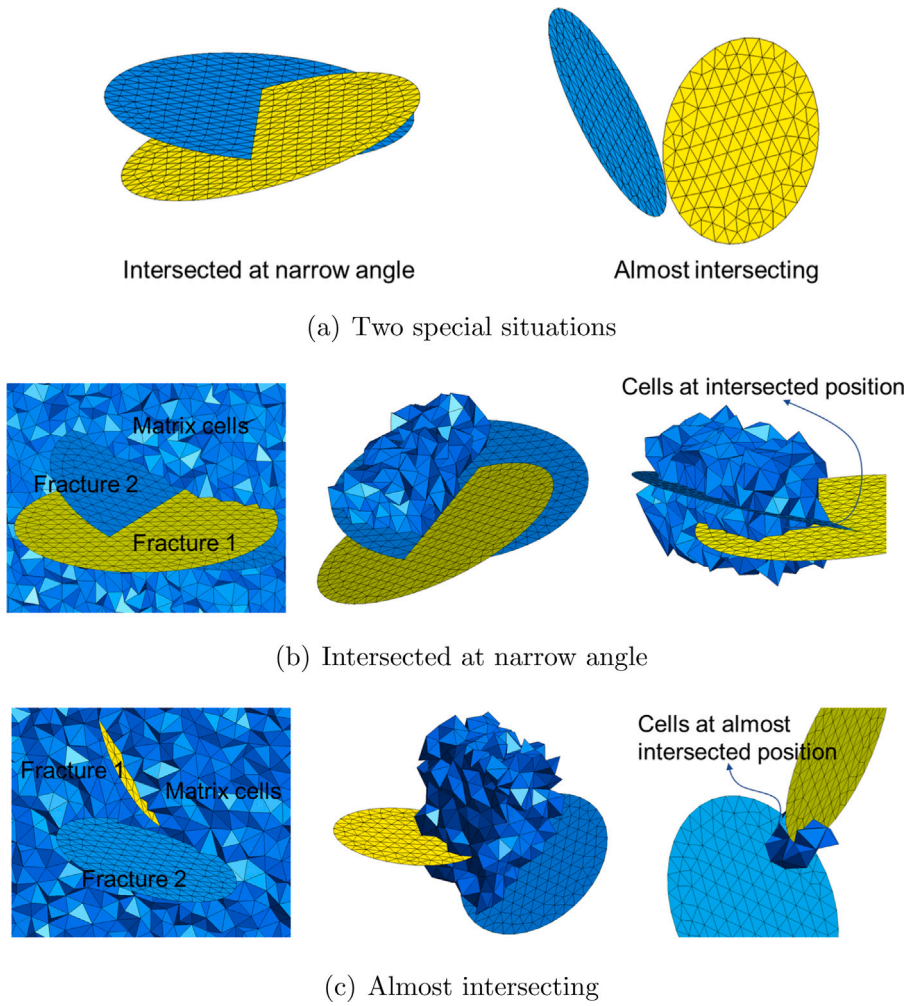

Fig. 5. Schematic of intersected fractures in two special situations.

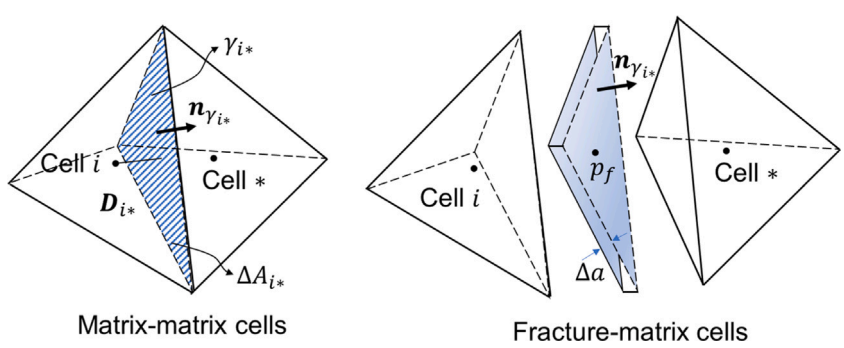

Fig. 6. Schematic of cell pairs and the parameters.

the intersected line is expressed by (Swokowski, 1979; Qiu, 2017):

$$\begin{pmatrix} A_i & B_i & C_i \\ A_j & B_j & C_j \end{pmatrix} \begin{pmatrix} x \\ y \\ z \end{pmatrix} = -\begin{pmatrix} D_i \\ D_j \end{pmatrix}, \quad (i \neq j) \tag{9}$$

The vector $\mathbf{m}_p$ parallel to this line is then obtained from Eq. (9), as displayed in Fig. 4a. It reads $\mathbf{m}_p = (D_p, E_p, F_p)$. The components are determined by the normal vectors of these two crossing fractures, $D_p = B_i C_j - C_i B_j$, $E_p = C_i A_j - A_i C_j$ and $F_p = A_i B_j - B_i A_j$. Then, the line is generated in the pre-processing stage to confine the cells in a conforming way. This effect can be observed in Fig. 4a.

Similarly, the treatment on the intersected fracture and inclusion is based on the equation of the intersected curve, as shown in Fig. 4b. This equation can be determined by combining Eqs. (4), (6) and (7). Therefore, the nodes are arranged along the intersected curve to ensure the conforming grids. An example is illustrated in Fig. 4b.

After defining all the constraints and geometrical entries in the computational domain, we could generate the grids. Fig. 3 illustrates several different patterns. It proves that the matrix cells are arranged along the fractures, where the fracture cells are placed at the interfaces of each of the matrix cell pairs. Furthermore, to show this meshing strategy is able to handle the extreme situations, typically where fractures are intersected at a narrow angle and almost intersecting, Fig. 5

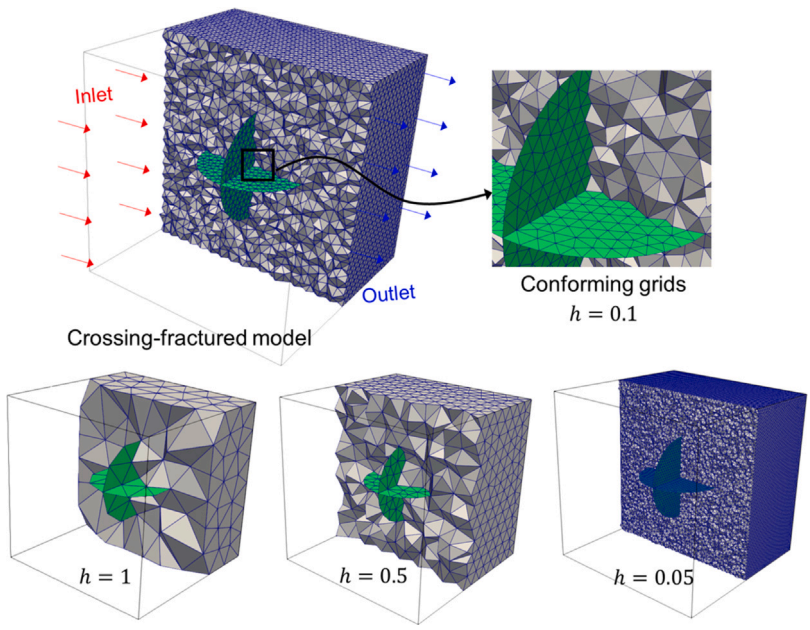

Fig. 7. The crossing-fractured model and meshes with different resolutions.

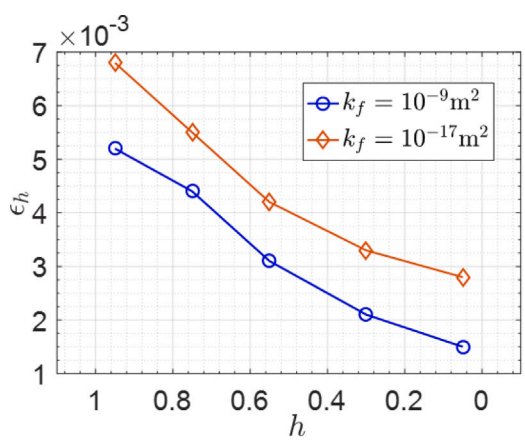

Fig. 8. Grid convergence of the 3D model with respect to the reference solution.

illustrates the grids of intersected fractures in two special situations. It is observed from Fig. 5b that grid refinement is carried out at the position that intersected at a narrow angle. Therefore, the conforming grids are arranged along the intersected fractures. These fractures provide the internal boundaries, as a constraint, for grid generation. As displayed in Fig. 5c, the finer grids are generated within the gap between these two fractures, which are almost intersected.

3. Governing equations and numerical method

3.1. Governing equations

Fluid flow in porous media is controlled by the law of mass conservation and Darcy's law (LeVeque, 1992; Wesseling, 2001). The general form of the governing equation reads:

$$\frac{\partial(\phi\rho)}{\partial t} + \nabla\cdot(\rho\mathbf{u}) = \rho q \tag{10}$$

where ρ is the density of fluid, μ the viscosity of fluid, ϕ the porosity of the porous medium, q the volumetric flux rate. The Darcy's velocity $\mathbf{u}$ in the medium, denoted $\mathbf{u}_m$, is determined by the Darcy's law:

$$\mathbf{u}_m = -\frac{\mathbf{k}_m}{\mu}\nabla p_m \tag{11}$$

where p_m is the fluid pressure within the rock bulk. $\mathbf{k}_m$ is the permeability tensor. For a heterogeneous medium, $\mathbf{k}_m$ is expressed by $k_{ij}, (i, j = x, y, z)$. For an isotropic medium, we denote $\mathbf{k}_m = k_m\mathbf{I}$, where $\mathbf{I}$ is the identity tensor.

In this work, we assume an incompressible fluid, therefore Eq. (10) reduces to a simplified form $\nabla\cdot\mathbf{u}_m = q$. Considering the flux interaction of fracture–matrix, the flux exchange term is expressed by $\mathbf{q}_{mf}\cdot\mathbf{n}_f$, where $\mathbf{q}_{mf}$ is the exchange of volumetric flux rate (Martin et al., 2005; Hyman et al., 2021). $\mathbf{n}_f$ is the unit normal vector of the interface between fracture–matrix.

Therefore, the governing equations of fluid flow in fractures are written as (Martin et al., 2005; Hyman et al., 2021):

$$\begin{aligned}\nabla\cdot\mathbf{u}_f &= -\left(\mathbf{q}_{mf}\cdot\mathbf{n}_f\right)\\ \mathbf{u}_f &= -\frac{k_f}{\mu}\nabla p_f\end{aligned} \tag{12}$$

where k_f is the permeability of fracture. $\mathbf{u}_f$ and p_f are the velocity and pressure within the fractures.

Consequently, at the interface of fracture–matrix, $\mathbf{q}_{mf}\cdot\mathbf{n}_f$ can be calculated by the pressure gradient between the matrix and fracture. The constraint required by mass conservation is naturally satisfied:

$$q_i V_i = \sum_{k=1}^{n_{nbi}} \mathbf{u}_k \Delta A_k \tag{13}$$

where ΔA_k is the area of interface between a cell pair. $\mathbf{u}_k$ is the velocity on the interface. n_{nbi} is the number of neighbors of cell i. V_i is volume of the cell. Therefore, the flux of interface k is $\mathbf{u}_k\Delta A_k$, where $\mathbf{u}_k$ is calculated by the pressure gradient according to the Darcy's law.

3.2. Models of fracture permeability

The permeability of fracture k_f shown in Eq. (12) is related to the characteristic dimension L or the aperture Δa of fracture. Here, we refer to two different models based on the relations of $k_f - L$ and $k_f - \Delta a$, respectively.

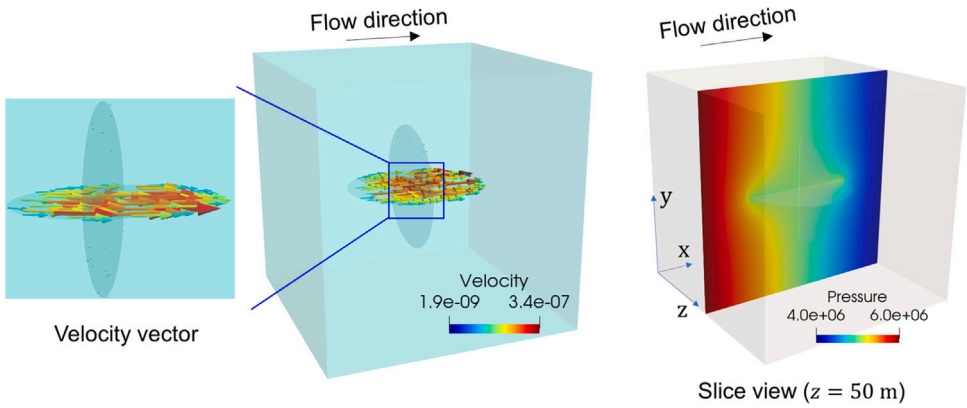

Fig. 9. Velocity (left) and pressure (right) distributions of the crossing-fractured model.

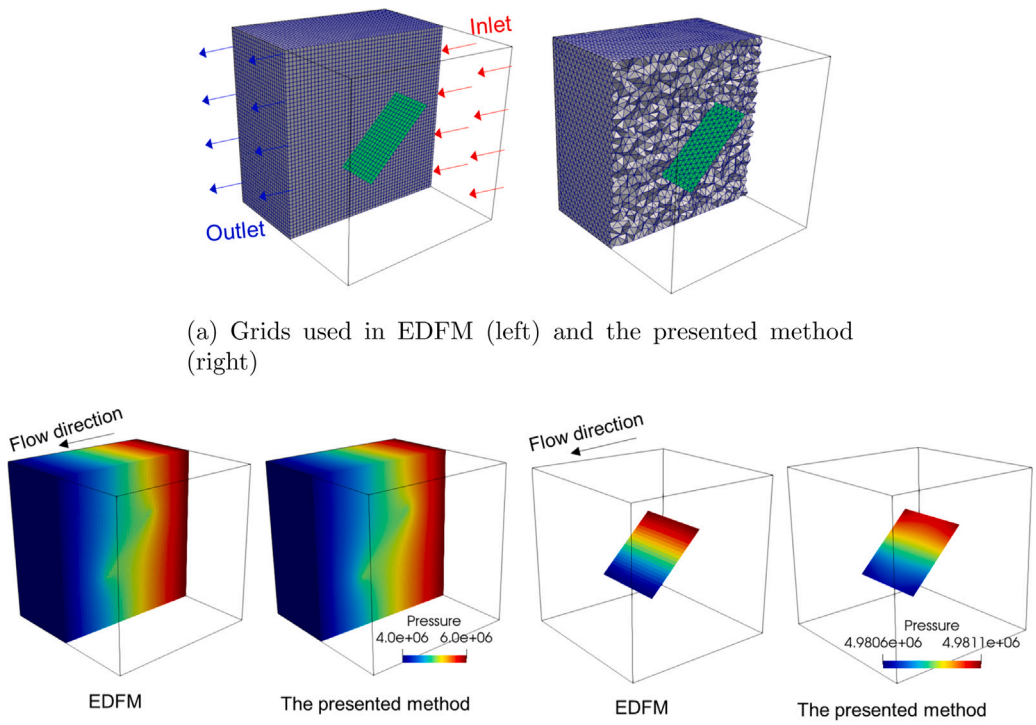

Fig. 10. Grids and simulation results of EDFM (by DARSim) and the presented method.

The classical cubic law provides the commonly used aperture-depended relation (Dippenaar and Van Rooy, 2016):

$$k_f = \frac{\Delta a^2}{12} \tag{14}$$

This form is simple and easy to implement. However, some studies have revealed that it needs corrections in some situations (Klimczak et al., 2010). Therefore, the dimension-depended relation has been proposed (Hyman et al., 2016). Here, we introduce the so-called correlated power law:

$$k_f = \lambda_1 L^{\lambda_2} \tag{15}$$

where λ_1 and λ_2 are the model parameters. In this work, as suggested by Hyman et al. (2016), λ_1 and λ_2 are set to 1.3×10^{-9} and 0.5, respectively. Based on the assumption of disk fracture, the characteristic dimension L is equal to the radius R.

Furthermore, a simplest model of fracture permeability is to assign a given value $\bar{k}_f$ to each of the fractures:

$$k_f = \bar{k}_f \tag{16}$$

Obviously, it can be seen from Eq. (15) that each of the fractures may have different k_f, since the radius R of each fracture is different. While as shown by Eq. (14), k_f is a constant if the aperture of each fracture is assumed as the same value. We will study the effect of different permeability models on hydraulic property in Section 4.

3.3. Numerical discretization

According to Eqs. (11), (12) and (13), the governing equations of the porous medium with multiple fractures and inclusions can be

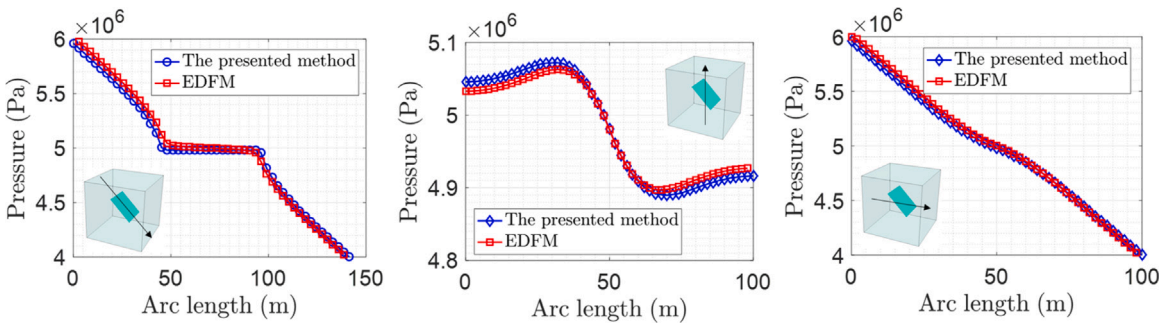

Fig. 11. Comparison of the pressure distributions calculated by EDFM (by DARSim) and the presented method.

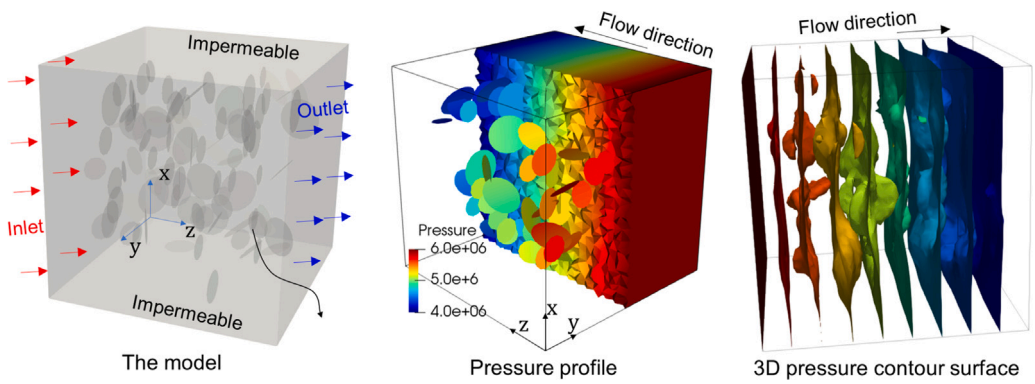

Fig. 12. Geometry of the random-fractured model and simulation results.

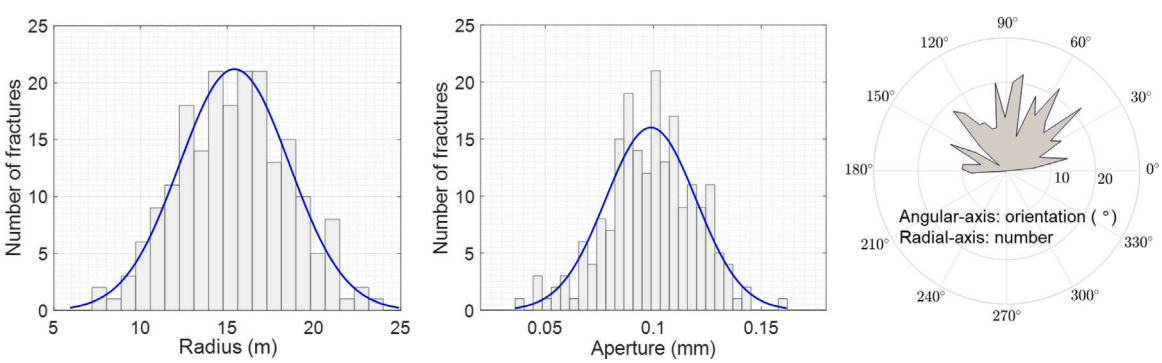

Fig. 13. Frequency distribution histograms of radius (left), aperture (middle) and orientation (right) of discrete fractures.

summarized as:

$$
\begin{aligned}
&-\nabla\cdot\left(\frac{\mathbf{k}_m}{\mu}\nabla p_m\right)=q_m,\\
&-\nabla\cdot\left(\frac{k_f}{\mu}\nabla p_f\right)=-\mathbf{q}_{mf}\cdot\mathbf{n}_f
\end{aligned}
\tag{17}
$$

The governing equation of seepage in inclusions is the same as that of the matrix, since they obey an unified numerical discretization scheme. Note that fluid flow in the inclusions follows Darcy's law in this work. Permeabilities of the inclusions and the matrix are allowed to be set to different values.

The primary unknown of Eq. (17) is fluid pressure (p_m, p_c and p_f), where the subscripts m, c and f represent the matrix, inclusion and fracture. In this work, numerical discretization is derived from the Galerkin finite element scheme (Wang, 2003; Zienkiewicz et al., 2013). For convenience, the unknown is denoted as p. The shape function is η_i, therefore the expression is given, $p \approx p_h = \sum_{i=1}^{n}\eta_i p_i$, where n is the total number of cells. Then, Eq. (17) is discretized cell-by-cell. This formulation will lead to the two-point flux approximation (TPFA) if the piece-wise constant function is selected ($\eta_i = 1$), as shown in the following discussion.

For a cell i, as shown in Fig. 6, the volume is V_i, and the neighbors are either fracture cells or matrix cells. The integral over cell i reads:

$$
\begin{aligned}
&\sum_{i=1}^{n_m}\int_{V_i}-\eta\nabla\cdot\left(\frac{\mathbf{k}_m}{\mu}\nabla p\right)dV=\int_{V_i}\eta q_m dV\\
&\sum_{i=1}^{n_f}\int_{V_i}-\eta\nabla\cdot\left(\frac{k_f}{\mu}\nabla p\right)dV=-\int_{V_i}\eta\left(\mathbf{q}_{mf}\cdot\mathbf{n}_f\right)dV
\end{aligned}
\tag{18}
$$

where n_m and n_f are the numbers of the matrix cells and fracture cells, respectively.

We then convert the volume integral at the left side of Eq. (18) to surface integral, to eliminate the divergence operation. Consequently,

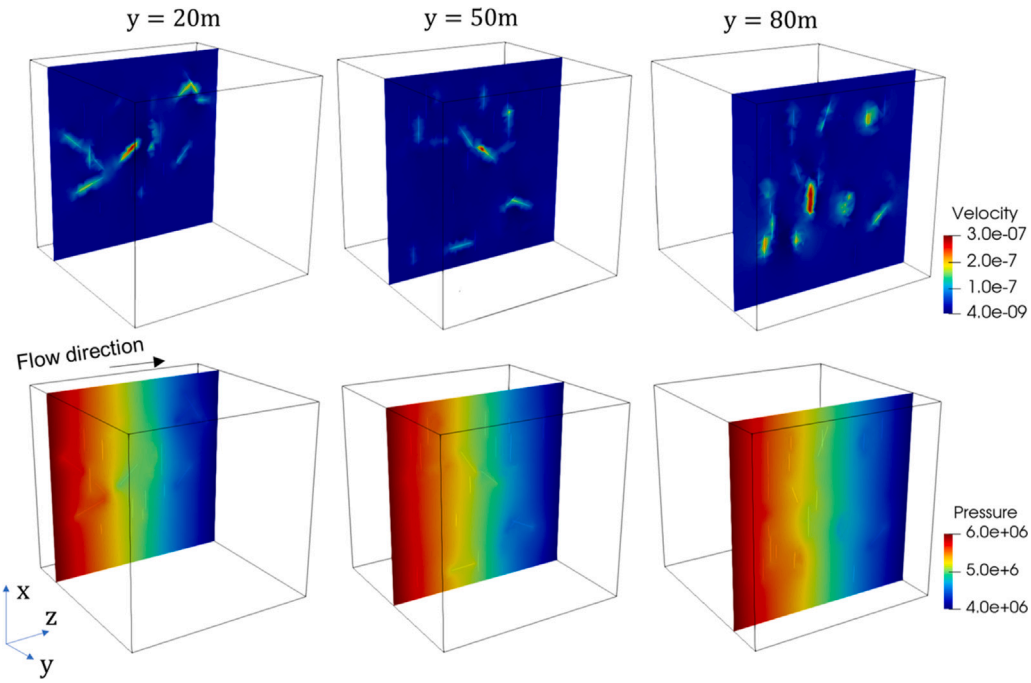

Fig. 14. Results of the random-fractured model. Velocity (top) and pressure (bottom) distributions at different slices along y-axis.

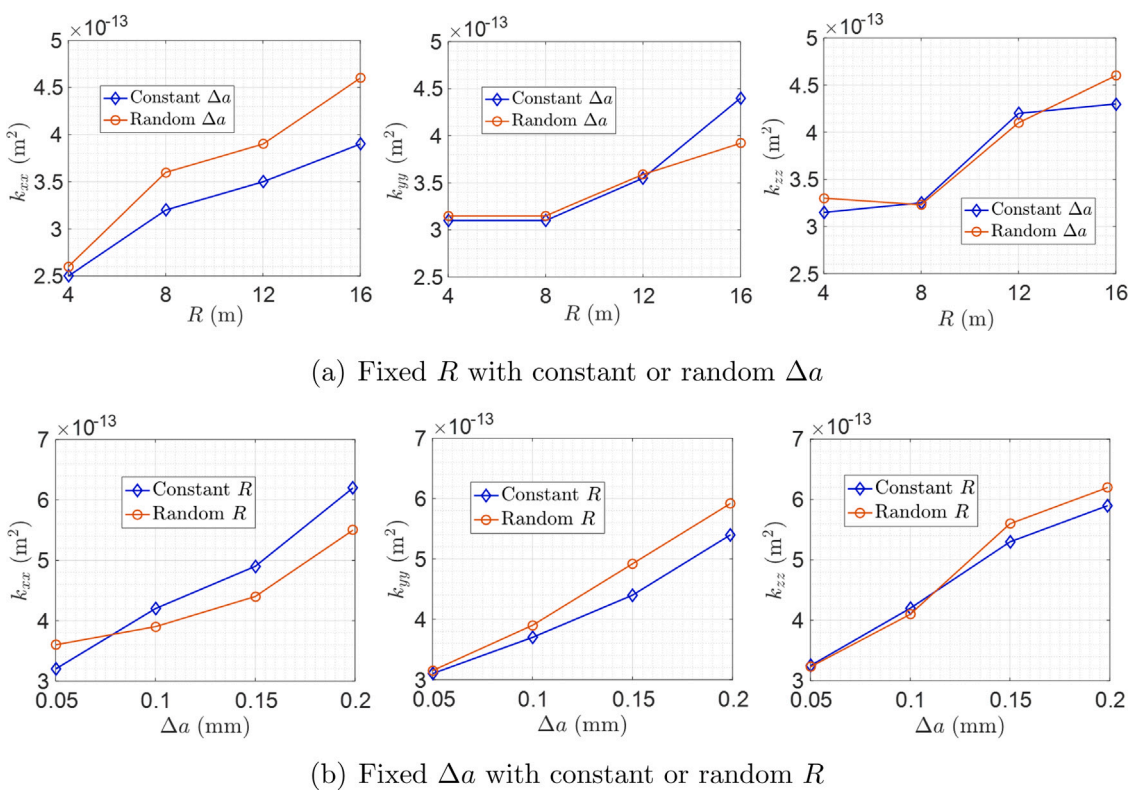

Fig. 15. The effect of fracture radius and aperture on the components of equivalent permeability tensor.

the discretized form for a matrix cell i is expressed as:

$$\sum_{*=1}^{n_{nbi}} \int_{\gamma_{i*}} -\eta \left(\frac{\mathbf{k}_m}{\mu} \nabla p \right) \cdot \mathbf{n}_{\gamma_{i*}} d\gamma = \int_{V_i} \eta q_m dV \tag{19}$$

where γ_{i*} is the interface between cell i and its neighbor $*$. The number of neighbors for cell i is n_{nbi}. $\mathbf{n}_{\gamma_{i*}}$ is the unit vector that points to the outward of interface γ_{i*}, as illustrated in Fig. 6.

For a fracture cell i, it reads:

$$\sum_{*=1}^{n_{nbi}} \int_{\gamma_{i*}} -\eta \left(\frac{k_f}{\mu} \nabla p \right) \cdot \mathbf{n}_{\gamma_{i*}} d\gamma = - \int_{V_i} \eta \left(\mathbf{q}_{mf} \cdot \mathbf{n}_f \right) dV \tag{20}$$

Applying Eqs. (19) and (20) to each of the cells, we use the finite difference scheme to approximate the pressure gradient ∇p. Note that

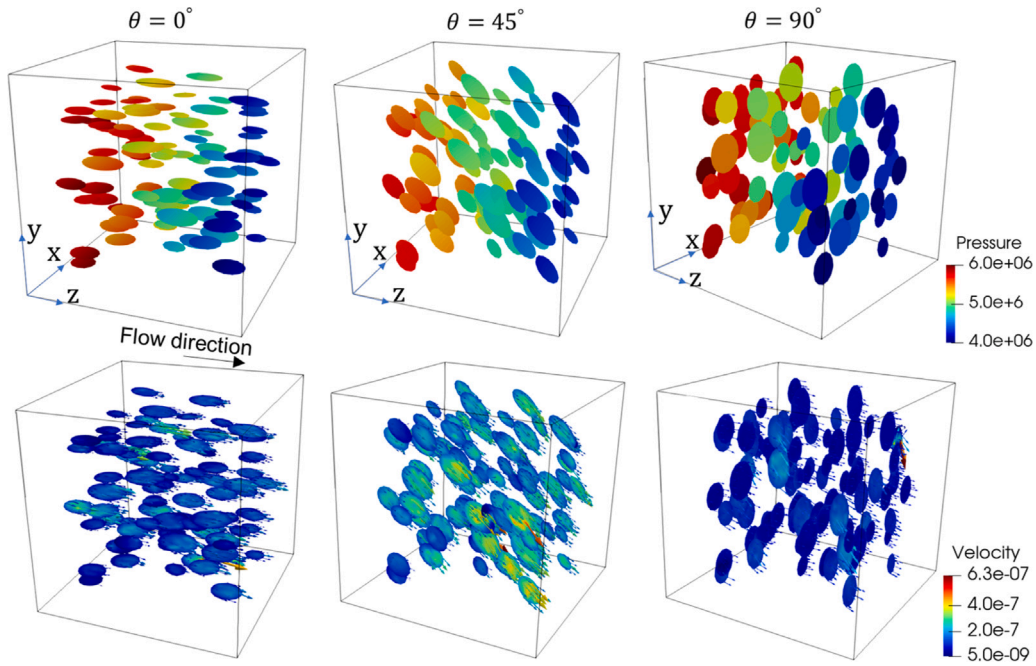

Fig. 16. The parallel-fractured models. Pressure profiles (top) and velocity vector field (bottom). Note that the rock matrix is hidden for visualization.

volume of cell i is ΔV_i. The shape function η_i equals to 1 once the piecewise constant function is selected. Therefore, the fully discretized forms of the matrix cells and fracture cells are expressed as:

$$\begin{aligned} &\sum_{*=1}^{n_{nbi}} T_{i*}\left(p_{mi}-p_*\right)=q_{mi}\Delta V_i \\ &\sum_{*=1}^{n_{nbi}} T_{i*}\left(p_{fi}-p_*\right)=-\left(\mathbf{q}_{mfi}\cdot\mathbf{n}_{fi}\right)\Delta V_i \end{aligned} \tag{21}$$

where T_{i*} is the transmissibility between cell i and cell $*$. T_{i*} is calculated by the half harmonic average $T_{i*}=\alpha_i\alpha_*/\left(\alpha_i+\alpha_*\right)$ as suggested in literature (Karimi-Fard et al., 2004; Stefansson et al., 2018). The sub-transmissibility α_i, in the case of anisotropic permeability, reads (Stefansson et al., 2018):

$$\alpha_i=\frac{\Delta A_{i*}\left(\mathbf{n}_{\gamma_{i*}}\cdot\mathbf{k}_i\right)}{\mathbf{D}_{i*}\cdot\mathbf{D}_{i*}}\cdot\mathbf{D}_{i*} \tag{22}$$

where $\mathbf{D}_{i*}$ is the distance vector from center of cell i to the interface sharing with cell $*$, as shown in Fig. 6. ΔA_{i*} is the area of the interface. We refer to Karimi-Fard et al. (2004) for the details of extension to intersected fractures.

After assembling all of the cells into one unified matrix, the algebraic system is written as:

$$\begin{bmatrix} \mathbf{T}_{mm} & \mathbf{T}_{mf} & \mathbf{T}_{mc} \\ \mathbf{T}_{fm} & \mathbf{T}_{ff} & \mathbf{T}_{fc} \\ \mathbf{T}_{cm} & \mathbf{T}_{cf} & \mathbf{T}_{cc} \end{bmatrix}\begin{bmatrix} \mathbf{p}_m \\ \mathbf{p}_f \\ \mathbf{p}_c \end{bmatrix}=\begin{bmatrix} \mathbf{Q}_m \\ \mathbf{Q}_f \\ \mathbf{Q}_c \end{bmatrix} \tag{23}$$

where $[\mathbf{p}_m,\mathbf{p}_f,\mathbf{p}_c]^{\mathrm{T}}$ is the unknown vector. $\mathbf{Q}_m$, $\mathbf{Q}_f$ and $\mathbf{Q}_c$ are the terms induced by the source. The coefficient matrix $\mathbf{T}_{ij}$ $(i,j=m,f,c)$ is composed by the transmissibility Eq. (22).

4. Numerical results and discussion

Numerical tests are conducted in this section to study the hydraulic properties of 3D fractured porous media. First, a crossing-fractured model and a single-fractured model are simulated for grid convergence evaluation and numerical validation. Then, the effects of heterogeneity and fracture parameters on seepage characteristics are investigated. Moreover, characteristics of a fractured medium with complex structures are analyzed.

4.1. Grid convergence evaluation and numerical validation

As shown in Fig. 7, two crossing fractures are placed at the center of the domain. The size of the domain is 100 m × 100 m × 100 m. The radius R of these two fractures is 25 m. The aperture Δa of fracture is 0.1 mm. We assume an isotropic medium in this test, therefore the permeability tensor of the rock matrix is $\mathbf{k}_m=k_m\mathbf{I}$, where $k_m=10^{-15}$ m^2. To simulate the fractures with highly conductive and low-permeability properties, the permeability of all fractures is set to $k_f=10^{-10}$ and 10^{-17} m^2.

The boundary conditions are prescribed-pressures on the right and left surfaces of the model, as shown in Fig. 7. The inlet is $p_{in}=6\times10^6$ Pa, and the outlet is $p_{out}=4\times10^6$ Pa. Other surfaces are impermeable.

Seepage in the fractured medium is simulated with different grid resolutions h. The meshes, with $h=1.0, 0.5, 0.1$ and 0.05, are displayed in Fig. 7. For instance, the model is partitioned using 112 397 tetrahedrons for the matrix, 840 triangles for the fractures and 21 031 nodes if $h=0.1$, and 8669 tetrahedrons, 2250 triangles and 1951 nodes if $h=0.5$. The convergence performance is provided in Fig. 8. The error ϵ_h is defined by:

$$\epsilon^h=\sum_{i=1}^{N_p}\frac{\left\|P_i-p_i^h\right\|_2}{\left\|P_i\right\|_2} \tag{24}$$

where P_i is the reference solution. p_i^h is the solution calculated by resolution h. N_p is the number of nodes selected to calculate the error.

As displayed in Fig. 8, it appears that the error gradually decreases with the increase of grid resolution. Furthermore, fracture permeability k_f shows an influence on convergence performance. The fractures with low-permeability lead to a relative higher error than the conductive fractures. The simulation results calculated by $h=0.1$ are shown in Fig. 9. It shows that the presence of fractures influences the pressure distribution as well as the velocity field. The velocity magnitude around the fractures is greater than that of in the rock matrix if the fractures play the role of conductive pathways.

Furthermore, to compare the simulation results obtained by our method with that of an existing method, a single-fractured model is created for this purpose. The computational domain and boundary conditions are the same as the above crossing-fractured model. As shown in Fig. 10, the single-fractured is a square with size 50 m × 50 m,

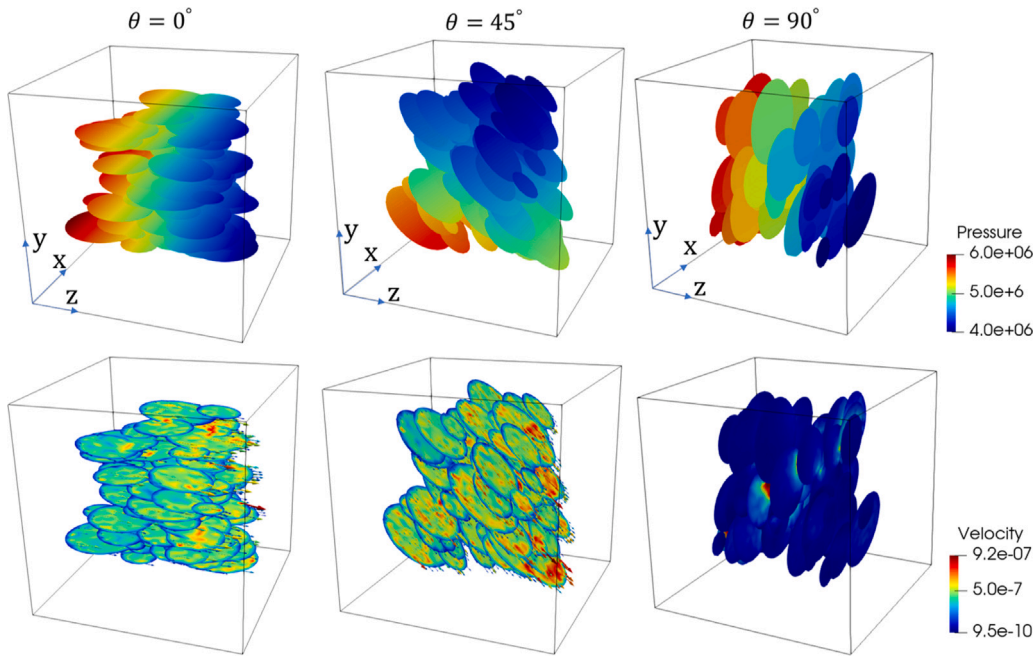

Fig. 17. The parallel-fractured models with multiple size fractures. Pressure profile (top) and velocity vector field (bottom). Note that the rock matrix is hidden for visualization.

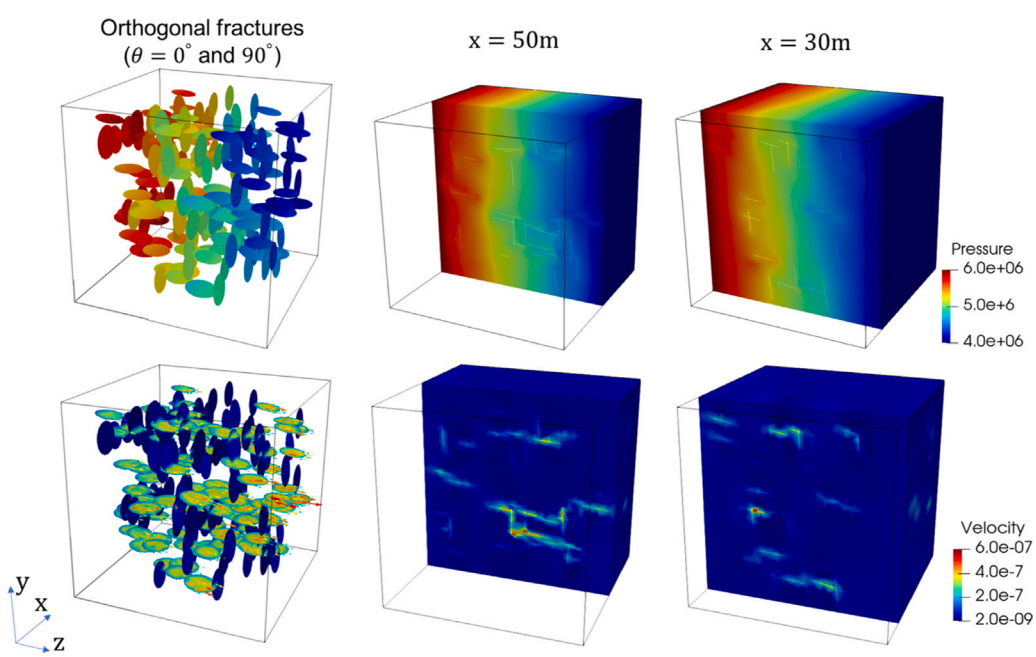

Fig. 18. The orthogonal-fractured model. Pressure profiles and the slice contours (top). Velocity vector field and the slice contours (bottom).

which is placed at the center of this domain with an inclined angle 45°. Permeabilities are $k_f = 10^{-10}$ m^2 and $k_m = 10^{-15}$ m^2. The simulation results calculated by the open source software DARSim (Hajibeygi et al., 2011; Ţene et al., 2017; Wang et al., 2022) are selected as a comparison to the results obtained by our method. The embedded discrete fracture model (EDFM) in DARSim uses the structured grids, where the grids of fracture and the matrix are independent, as displayed in Fig. 10a. The gravity effect is neglected in this test. Simulation results are shown in Fig. 10b. It demonstrates a good matching between the solutions calculated by the presented method and EDFM. In addition, Fig. 11 provides the additional results to illustrate this point. The results of comparison prove that the presented method is reliable and accurate.

4.2. A fractured porous medium with different geometrical patterns

To investigate the effect of geometrical parameters of fractures, the random-fractured model and the parallel-fractured model are simulated with different radius, orientation and aperture distributions. The size of this domain and boundary conditions are the same as the settings in Section 4.1.

The random-fractured model is displayed in Fig. 12. Both the fractures and the rock matrix are meshed as shown in this figure, therefore the flux connection of matrix-fractures is described by the governing equations of fluid flow in fractured porous model Eq. (17). We assign the randomly distributed radius R and aperture Δa to each of the fractures. Therefore, the fracture permeability depends on the aperture, where the $k_f - \Delta a$ relation Eq. (14) is adopted.

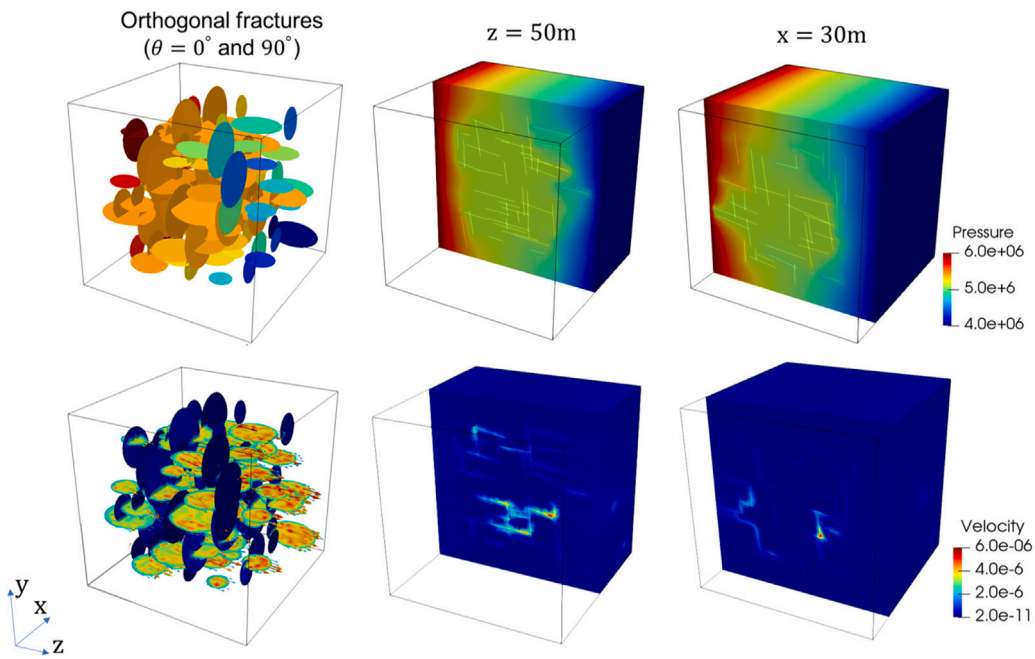

Fig. 19. The orthogonal-fractured model with multiple size fractures. Pressure profiles and the slice contours (top). Velocity vector field and the slice contours (bottom).

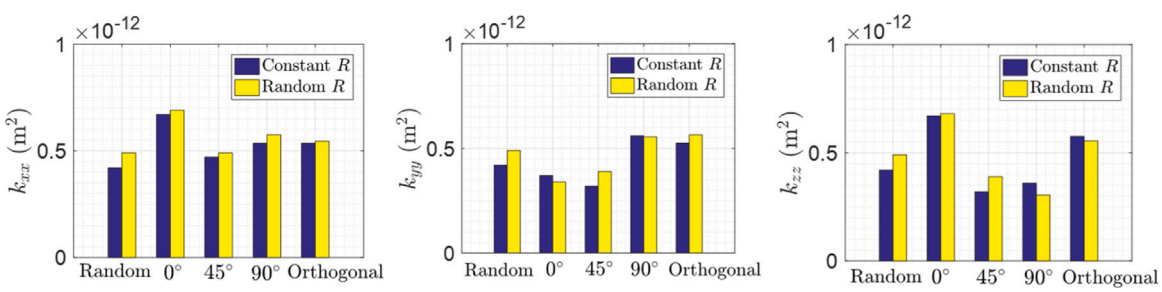

Fig. 20. The effect of fracture orientation on permeability.

Fig. 13 provides the frequency distribution histograms of these parameters. The number of fractures distributed in the medium is $N_f = 200$. Furthermore, Fig. 13 illustrates the frequency distribution histograms of fracture orientation, where the radial-axis represents the number of fractures and the angular-axis is the orientation. We compare the distributions of velocity and pressure at different slices, as displayed in Fig. 14. The presence of fractures induces the conductive pathways. It is appears that the velocity magnitude in the fracture medium is on the order of $1 \times 10^{-9} \sim 10^{-7}$ m/ s, which is consistent with the experimental studies (Jung et al., 2012).

To analyze the effect of radius R and aperture Δa on permeability, we compare the variation of the components of the equivalent permeability tensor with respect to the radius, as shown in Fig. 15a. The constant aperture is equal to 0.1 mm in this case, while the distribution of the random aperture is shown in Fig. 13. In addition, the comparison between the random radius and constant radius is shown in Fig. 15b, where the constant radius is set to 15 m.

A fractured medium with parallel fractures and orthogonal fractures is simulated. We select different orientations of the fractures, $\theta = 0°, 45°$ and 90°. The simulation results are shown in Fig. 16 for constant radius and Fig. 17 for random radius. In addition, the orthogonal fractures are simulated with different size of the fractures, as displayed in Figs. 18 and 19. The slice contours show that the effect of large-size fractures, on pressure distribution as well as the velocity magnitude, is relatively larger than that of the small-size fractures, due to the large-size fractures play a dominant role in the seepage process. We compare the components of the equivalent permeability tensor, as illustrated in Fig. 20. Note that the inlet and outlet are imposed on the left and right surfaces, respectively. Therefore, the flow direction is along z-axis. The orientation of the parallel fractures is measured with respect to z-axis. Consequently, k_{xx} and k_{zz} are relatively larger than k_{yy} in the situation of $\theta = 0°$. Similarly, k_{xx} and k_{yy} are relatively larger than k_{zz} in the situation of $\theta = 90°$.

4.3. The effects of heterogeneity and permeability models

To analyze the effect of hydraulic property on fluid flow, the random permeability fields are generated to reproduce the heterogeneous characteristic, as shown in Fig. 21. Boundary conditions are the same as in Section 4.2. The aperture of fractures is set to 0.1 mm. We compare the pressure distribution along the flow direction, as shown in Fig. 22. It shows that the orientation of fractures influences the pressure distribution. Especially, it is observed that the curve of $\theta = 0°$ shows a flat shape in the middle. The reason is that the parallel fractures play the role of conductive pathways, therefore the fluid directly flows through the fracture networks.

Furthermore, the permeability model of fractures has influence on pressure distribution. We simulate seepage using three different permeability models, namely the cubic law Eq. (14), the correlated power law (15) and the random permeability show in Fig. 21. We calculate the pressure deviation of these three models with respect to the constant model Eq. (16). The results are shown in Fig. 22. It shows

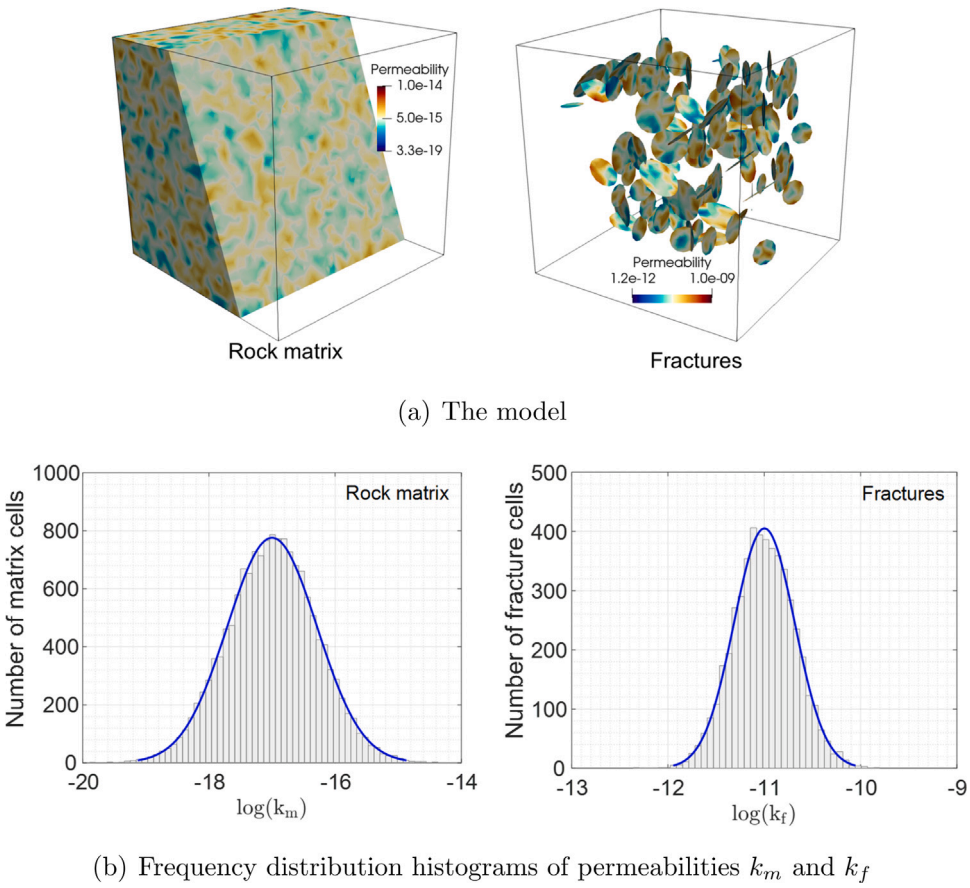

Fig. 21. Permeability field of the heterogeneous fractured porous medium.

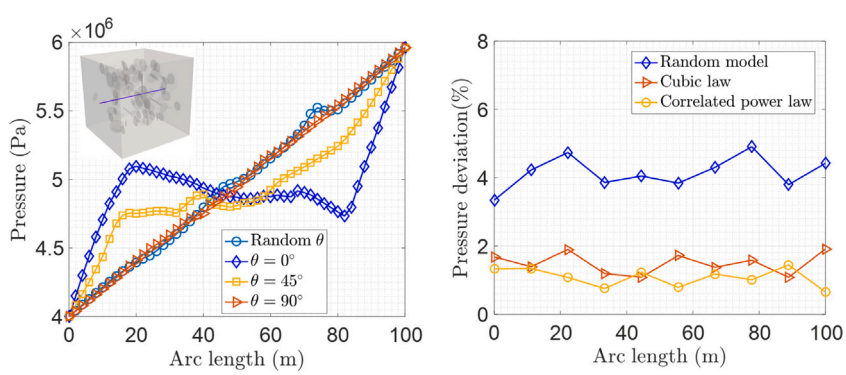

Fig. 22. Pressure distribution along a survey line crossing the domain (left). Pressure deviation induced by different permeability models with respect to the constant model (right).

that the random model exhibits a relative large deviation compared to other models, while the solutions calculated by the cubic law and the correlated power law are very close.

The effect of heterogeneity on pressure distribution is illustrated in Fig. 23. It shows that the presence of heterogeneous permeability, as shown in Fig. 21, produces a small fluctuation on pressure distribution. However, the tendencies of pressure variation in the situations of heterogeneity and homogeneity are very close. Therefore, the influence of heterogeneity on seepage is relatively smaller than that of fracture orientation.

4.4. A fractured porous medium with complex structures

In practice, there are many discrete fractures and inclusions distributed inside the geological fields (Huang et al., 2011; Aliouache et al., 2019; Wang et al., 2022c). They have significant influence on fluid flow in the fractured porous medium. In this section, we simulate three different patterns with the complex structures. As shown in Fig. 24, Patterns 1 and 2 consider both fractures and inclusions. The radii of inclusions R_c and fractures R_f in Pattern 1 are 5 ~ 10 m. In Pattern 2, both R_c and R_f are 10 ~ 15 m. In Pattern 3, R_c is 6 ~ 8 m.

The size of the domain and the boundary conditions are the same as in Section 4.3. The permeabilities of the inclusions and fractures are set to $k_c = 1 \times 10^{-10}$ m^2 and $k_f = 1 \times 10^{-10}$ m^2, respectively. The permeability of the rock matrix is $k_m = 1 \times 10^{-15}$ m^2. Therefore, the fractures and inclusions play the role of conductive pathways. Both the fractures, inclusions and the matrix are meshed, as displayed in Fig. 24. It can be seen that the velocity magnitude in the fractures is relatively larger than in the inclusions. The reason is that the pressure gradient around the interface between fractures and matrix is greater than that of around the interface between inclusions and matrix.

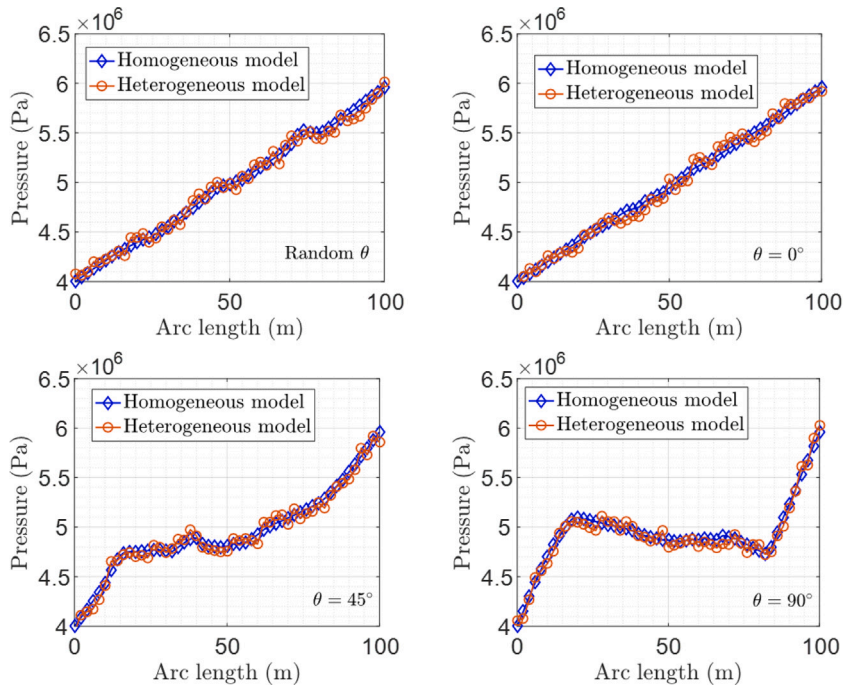

Fig. 23. Comparison of pressure distribution between heterogeneous and homogeneous models with different fracture orientations.

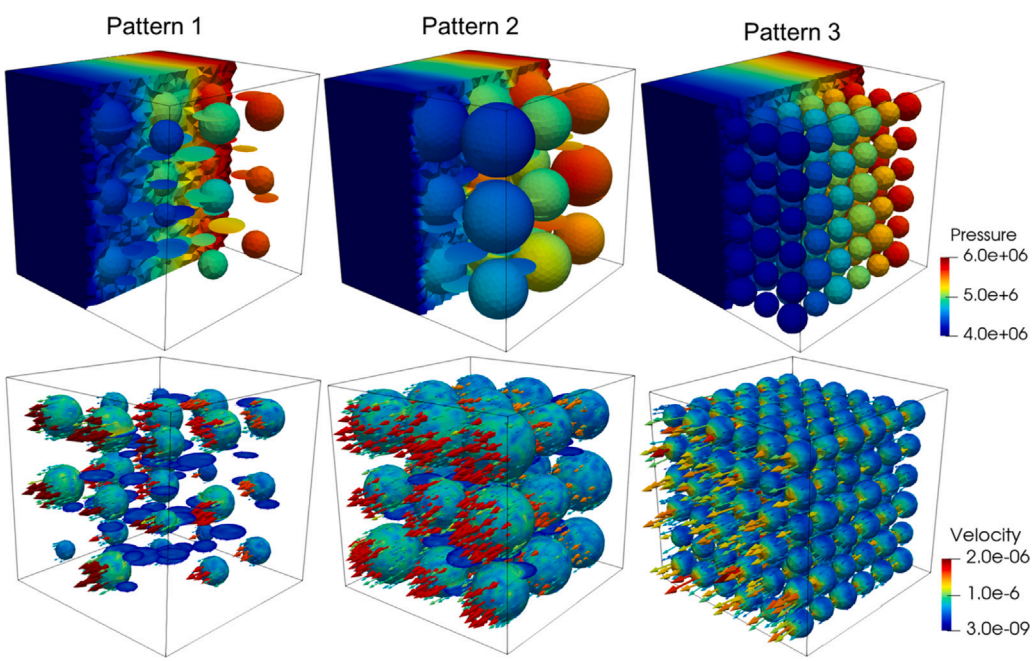

Fig. 24. Pressure distribution (top row) and velocity vector field (bottom row) of the model with three different patterns.

To analyze the effect of fractures and inclusions on permeability, the components of the equivalent permeability tensor are calculated, as shown in Fig. 25. It appears that k_{xx}, k_{yy} and k_{zz} are increased with the increase of fracture number. However, the increasing rate of permeability in Pattern 3 is relatively smaller than in Patterns 1 and 2, since the effect of inclusions on seepage is smaller than that of the fractures.

Then, we generate the heterogeneous permeability field, which is the same as Fig. 21. Fig. 26 provides the comparison of pressure distribution between the heterogeneous model and the homogeneous model. It is found that the oscillation of pressure is induced by the heterogeneity. The discontinuities of the pressure distribution is produced by the presence of inclusions and fractures.

Later, in Pattern 3, the permeability of the rock matrix k_m is set to 1×10^{-15} m^2, while that of the inclusions k_c is set to two different values 1×10^{-10} and 1×10^{-20} m^2, to simulate the conductive pathways and the barriers. We compare the distribution of velocity along the flow direction in these two situations, as shown in Fig. 27. It appears that the variation of velocity magnitude shows a regular shape, since the presence of the inclusions influences pressure distribution. The inclusions with low-permeability produce a low speed of seepage, which is on the order of 1×10^{-8} m/s. The velocity magnitude reaches the maximum

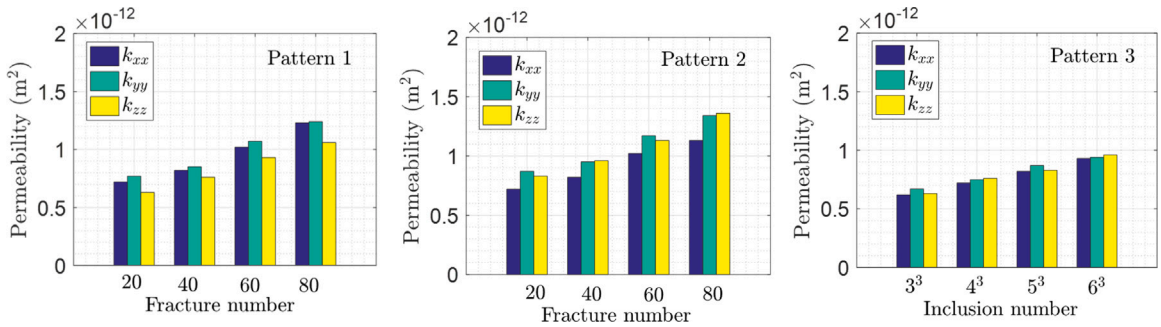

Fig. 25. Variation of the components of equivalent permeability tensor with different patterns.

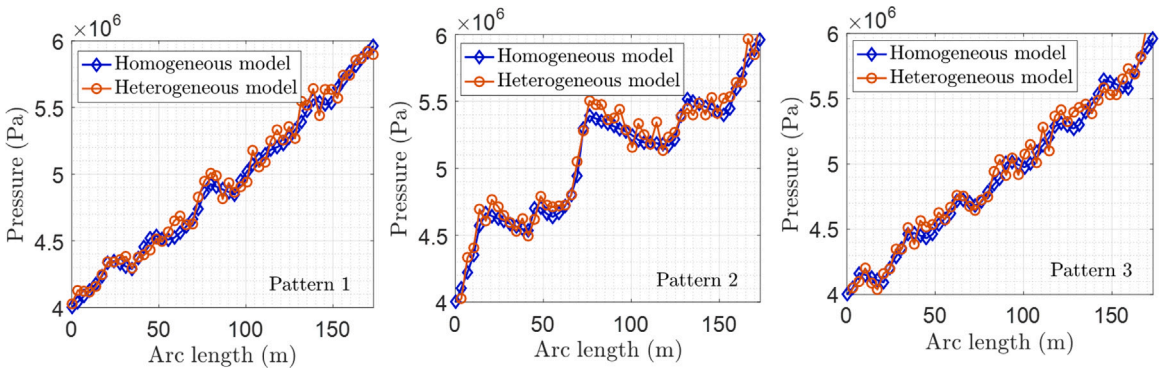

Fig. 26. Comparison of pressure distribution along the diagonal of the model with different patterns.

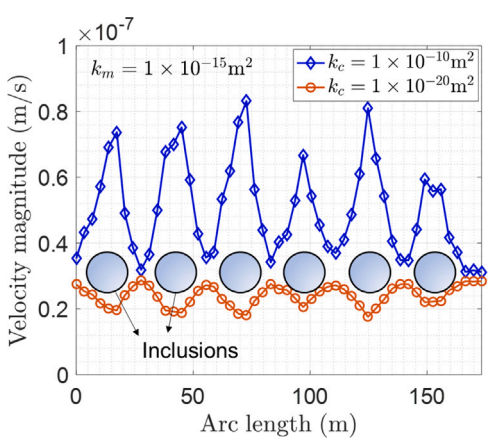

Fig. 27. Comparison of velocity magnitude distribution of low-permeability and conductive inclusions.

value at the center of the inclusions if the inclusions are modeled as the conductive pathways.

5. Conclusions

This work investigates numerical modeling approach for seepage in heterogeneous porous media with complex structures, especially the discrete fractures and the inclusions. Based on the presented method, we analyze the characteristics of heterogeneous fractured porous media, to study the effect of different patterns of these structures on seepage process. The main concluding remarks are drawn below.

(1) To generate the randomly distributed geometrical structures, a modeling approach of the 3D fractures and inclusions is introduced based on the analytic geometry. Therefore, a fractured porous medium is decomposed into three components, namely the rock matrix, fractures and inclusions. The geometrical parameters, including the radius, coordinates and orientation of discrete fractures, are generated by a statistical approach.

(2) A meshing strategy is introduced to partition the geometry. Especially, the treatment on intersected elements is discussed. The extreme situations, typically where fractures are intersected at a narrow angle and almost intersecting, are discussed to show the capacity of this meshing strategy. On the other hand, the governing equations of fluid flow are discretized by the TPFA, in which the flux connections of fractures, inclusions and the rock matrix are considered.

(3) A series of numerical tests is carried out to analyze the hydraulic characteristics of the 3D fractured porous media. The crossing-fractured model is simulated with different grid resolutions, to evaluate the convergence performance of this modeling method. A single-fractured model is used to validate the developed conforming model by comparing simulation results obtained using the nonconforming EDFM. Next, models with random and parallel fractures are simulated to investigate the effect of aperture and radius of fractures on seepage.

(4) The effect of the heterogeneity and permeability model on seepage is studied. It shows that the random model exhibits a relative large deviation compared to other models, while the solutions calculated by the cubic law and the correlated power law are very close. Finally, the hydraulic properties of a fractured porous medium with complex structures are investigated. It appears that the presence of heterogeneous permeability produces small fluctuations on pressure distribution. The velocity magnitude in the fractures is relatively larger than in the inclusions. The reason is that the pressure gradient around the interface between fractures–matrix is greater than that of around the interface between inclusions–matrix. The velocity magnitude reaches the maximum value at the center of the inclusions if the inclusions are modeled as the conductive pathways.

Several extensions of the current framework deserve further investigations. Especially, adaptation of a grid optimization approach is required in order to address a wide range of cases in which k-orthogonality is not preserved (Karimi-Fard, 2008; Karimi-Fard and

Durlofsky, 2016). Furthermore, extensions to hydro-mechanical coupling and fracture propagation processes are key aspects in dealing with deformation within the porous structure. Therefore, another promising extension is to combine the discrete element method with the presented continuum-scale model (Yan et al., 2018; Knight et al., 2020), to achieve the simulation of hydro-mechanical processes in 3D deformable fractured media with complex structures.

CRediT authorship contribution statement

Luyu Wang: Conceptualization, Methodology, Software, Writing – original draft. **Yuhang Wang:** Validation, Writing – review & editing. **Cornelis Vuik:** Writing – review & editing. **Hadi Hajibeygi:** Funding acquisition, Writing – review & editing.

Declaration of competing interest

The authors declare that they have no known competing financial interests or personal relationships that could have appeared to influence the work reported in this paper.

Acknowledgments

Hadi Hajibeygi was sponsored by the NWO-TTW ViDi grant (project ADMIRE 17509). The authors would like to thank the group members of DARSim (Delft Advanced Reservoir Simulation) and ADMIRE (Adaptive Dynamic Multiscale Integrated Reservoir Earth) at TU Delft for the fruitful discussions.

References

Adler, P.M., Thovert, J.F., Mourzenko, V.V., 2013. Fractured Porous Media. Oxford University Press, United Kingdom, http://dx.doi.org/10.1093/acprof:oso/9780199666515.001.0001.

Ahmed, R., Edwards, M.G., Lamine, S., Huisman, B.A.H., Pal, M., 2015. Three-dimensional control-volume distributed multi-point flux approximation coupled with a lower-dimensional surface fracture model. J. Comput. Phys. 303, 470–497. http://dx.doi.org/10.1016/j.jcp.2015.10.001.

Aliouache, M., Wang, X., Jourde, H., Huang, Z., Yao, J., 2019. Incipient karst formation in carbonate rocks: Influence of fracture network topology. J. Hydrol 575, 824–837. http://dx.doi.org/10.1016/j.jhydrol.2019.05.082.

Berkowitz, B., 2002. Characterizing flow and transport in fractured geological media: A review. Adv. Water Resour. 25, 861–884. http://dx.doi.org/10.1016/S0309-1708(02)00042-8.

Bilke, L., Flemisch, B., Kalbacher, T., Kolditz, O., Helmig, R., Nagel, T., 2019. Development of open-source porous media simulators: Principles and experiences. Transp. Porous Media 130, 337–361. http://dx.doi.org/10.1007/s11242-019-01310-1.

Cacas, M.C., Ledoux, E., de Marsily, G., Tillie, B., Barbreau, A., Durand, E., Feuga, B., Peaudecerf, P., 1990. Modeling fracture flow with a stochastic discrete fracture network: calibration and validation: 1. The flow model. Water Resour. Res. 26 (3), 479–489. http://dx.doi.org/10.1029/WR026i003p00479.

Cañamón, I., Rajeh, T., Ababou, R., Marcoux, M., 2022. Topological analysis of 3D fracture networks: Graph representation and percolation threshold. Comput. Geotech. 142, 104556. http://dx.doi.org/10.1016/j.compgeo.2021.104556.

Chung, E.T., Efendiev, Y., Leung, W.T., Vasilyeva, M., Wang, Y., 2018. Non-local multi-continua upscaling for flows in heterogeneous fractured media. J. Comput. Phys. 372, 22–34. http://dx.doi.org/10.1016/j.jcp.2018.05.038.

de Dreuzy, J.R., Pichot, G., Poirriez, B., Erhel, J., 2013. Synthetic benchmark for modeling flow in 3D fractured media. Comput. Geosci. 50, 59–71. http://dx.doi.org/10.1016/j.cageo.2012.07.025.

Dershowitz, W.S., Fidelibus, C., 1999. Derivation of equivalent pipe network analogues for three-dimensional discrete fracture networks by the boundary element method. Water Resour. Res. 35 (9), 2685–2691. http://dx.doi.org/10.1029/1999WR900118.

Dippenaar, M.A., Van Rooy, J.L., 2016. On the cubic law and variably saturated flow through discrete open rough-walled discontinuities. Int. J. Rock Mech. Min. Sci. 89, 200–211. http://dx.doi.org/10.1016/j.ijrmms.2016.09.011.

Ghahfarokhi, P.K., 2017. The structured gridding implications for upscaling model discrete fracture networks (DFN) using corrected Oda's method. J. Pet. Sci. Eng. 153, 70–80. http://dx.doi.org/10.1016/j.petrol.2017.03.027.

Hajibeygi, H., Karvounis, D., Jenny, P., 2011. A hierarchical fracture model for the iterative multiscale finite volume method. J. Comput. Phys. 230 (24), 8729–8743. http://dx.doi.org/10.1016/j.jcp.2011.08.021.

Hajibeygi, H., Olivares, M.B., HosseiniMehr, M., Pop, S., Wheeler, M., 2020. A benchmark study of the multiscale and homogenization methods for fully implicit multiphase flow simulations. Adv. Water Resour. 143, 103674. http://dx.doi.org/10.1016/j.advwatres.2020.103674.

Huang, N., Liu, R., Jiang, Y., Cheng, Y., 2021. Development and application of three-dimensional discrete fracture network modeling approach for fluid flow in fractured rock masses. J. Nat. Gas Sci. Eng. 103957. http://dx.doi.org/10.1016/j.jngse.2021.103957.

Huang, Z., Yao, J., Li, Y., Wang, C., Lv, X., 2011. Numerical calculation of equivalent permeability tensor for fractured vuggy porous media based on homogenization theory. Commun. Comput. Phys. 9 (1), 180–204. http://dx.doi.org/10.4208/cicp.150709.130410a.

Hyman, J.D., Aldrich, G., Viswanathan, H., Makedonska, N., Karra, S., 2016. Fracture size and transmissivity correlations: Implications for transport simulations in sparse three-dimensional discrete fracture networks following a truncated power law distribution of fracture size. Water Resour. Res. 52 (8), 6472–6489. http://dx.doi.org/10.1002/2016WR018806.

Hyman, J.D., Gable, C.W., Painter, S.L., Makedonska, N., 2014. Conforming delaunay triangulation of stochastically generated three dimensional discrete fracture networks: A feature rejection algorithm for meshing strategy. SIAM J. Sci. Comput. 36, A1871–A1894. http://dx.doi.org/10.1137/130942541.

Hyman, J.D., Karra, S., Makedonska, N., Gable, C.W., Painter, S.L., Viswanathan, H.S., 2015. DfnWorks: A discrete fracture network framework for modeling subsurface flow and transport. Comput. Geosci. 84, 10–19. http://dx.doi.org/10.1016/j.cageo.2015.08.001.

Hyman, J.D., Sweeney, M.R., Gable, C.W., Svyatsky, D., Lipnikov, K., Moulton, J.D., 2021. Flow and transport in three-dimensional discrete fracture matrix models using mimetic finite difference on a conforming multi-dimensional mesh. http://dx.doi.org/10.48550/arXiv.2112.12592, arXiv preprint arXiv:2112.12592.

Jacquemyn, C., Pataki, M.E.H., Hampson, G.J., Jackson, M.D., Petrovskyy, D., Geiger, S., Marques, C.C., Machado Silva, J.D., Judice, S., Rahman, F., Costa Sousa, M., 2021. Sketch-based interface and modeling of stratigraphy and structure in three dimensions. J. Geol. Soc. Lond. 178 (4), jgs2020–187. http://dx.doi.org/10.1144/jgs2020-187.

Jung, S.Y., Lim, S., Lee, S.J., 2012. Investigation of water seepage through porous media using X-ray imaging technique. J. Hydrol. 425, 83–89. http://dx.doi.org/10.1016/j.jhydrol.2012.05.034.

Karimi-Fard, M., 2008. Grid optimization to improve orthogonality of two-point flux approximation for unstructured 3D fractured reservoirs. In: ECMOR 2008-11th European Conference on the Mathematics of Oil Recovery. http://dx.doi.org/10.3997/2214-4609.20146380.

Karimi-Fard, M., Durlofsky, L.J., 2012. Accurate resolution of near-well effects in upscaled models using flow-based unstructured local grid refinement. SPE J. 17 (4), 1084–1095. http://dx.doi.org/10.2118/141675-PA.

Karimi-Fard, M., Durlofsky, L.J., 2016. A general gridding, discretization, and coarsening methodology for modeling flow in porous formations with discrete geological features. Adv. Water Resour. 96, 354–372. http://dx.doi.org/10.1016/j.advwatres.2016.07.019, 2016.

Karimi-Fard, M., Durlofsky, L.J., Aziz, K., 2004. An efficient discrete-fracture model applicable for general-purpose reservoir simulators. SPE J 9, 227–236. http://dx.doi.org/10.2118/88812-PA.

Klimczak, C., Schultz, R.A., Parashar, R., Reeves, D.M., 2010. Cubic law with aperture-length correlation: implications for network scale fluid flow. Hydrogeol. J. 18, 851–862. http://dx.doi.org/10.1007/s10040-009-0572-6.

Knight, E.E., Rougier, E., Lei, Z., Euser, B., Chau, V., Boyce, S.H., Gao, K., Okubo, K., Froment, M., 2020. HOSS: an implementation of the combined finite-discrete element method. Comput. Part. Mech. 7, 765–787. http://dx.doi.org/10.1007/s40571-020-00349-y.

Kolditz, O., Görke, U.J., Shao, H., Wang, W., 2012. Thermo-Hydro-Mechanical–Chemical Processes in Fractured Porous Media. Springer Science & Business Media.

LeVeque, R.J., 1992. Numerical Methods for Conservation Laws. Birkhäuser, Basel.

Martin, V., Jaffré, J., Roberts, J.E., 2005. Modeling fractures and barriers as interfaces for flow in porous media. SIAM J. Sci. Comput. 26 (5), 667–1691. http://dx.doi.org/10.1137/S1064827503429363.

Mejia, C., Roehl, D., Rueda, J., Quevedo, R., 2021. A new approach for modeling three-dimensional fractured reservoirs with embedded complex fracture networks. Comput. Geotech. 130, 103928. http://dx.doi.org/10.1016/j.compgeo.2020.103928.

Mustapha, H., Dimitrakopoulos, R., Graf, T., Firoozabadi, A., 2011. An efficient method for discretizing 3D fractured media for subsurface flow and transport simulations. Internat. J. Numer. Methods Fluids 67, 651–670. http://dx.doi.org/10.1002/fld.2383.

Qiu, W.S., 2017. Analytic Geometry. Peking University Press, Beijing.

Shewchuk, J.R., 2002. Delaunay refinement algorithms for triangular mesh generation. Comput. Geom. Theory Appl. 22, 21–74. http://dx.doi.org/10.1016/S0925-7721(01)00047-5.

Stefansson, I., Berre, I., Keilegavlen, E., 2018. Finite-volume discretisations for flow in fractured porous media. Transp. Porous Media 124, 439–462. http://dx.doi.org/10.1007/s11242-018-1077-3.

Sui, Q., Chen, W., Wang, L., 2022. Investigation of nonlinear flow in discrete fracture networks using an improved hydro-mechanical coupling model. Appl. Sci. 12 (6), 3027. http://dx.doi.org/10.3390/app12063027.

Swokowski, E.W., 1979. Calculus with Analytic Geometry. Taylor & Francis, Boston.

Tan, X., Chen, W., Wang, L., Yang, J., Tan, X., 2021. Settlement behaviors investigation for underwater tunnel considering the impacts of fractured medium and water pressure. Mar. Georesour. Geotechnol. 39 (6), 639–648. http://dx.doi.org/10.1080/1064119X.2020.1737279.

Şene, M., Bosma, S.B.M., Al Kobaisi, M.S., Hajibeygi, H., 2017. Projection-based embedded discrete fracture model (pEDFM). Adv. Water Resour. 105, 205–216. http://dx.doi.org/10.1016/j.advwatres.2017.05.009.

Wang, X., 2003. Finite Element Method. Tsinghua University Press, Beijing.

Wang, L., Chen, W., Tan, X., Tan, X., Yang, J., Yang, D., Zhang, X., 2020. Numerical investigation on the stability of deforming fractured rocks using discrete fracture networks: a case study of underground excavation. Bull. Eng. Geol. Environ. 79, 133–151. http://dx.doi.org/10.1007/s10064-019-01536-9.

Wang, L., Chen, W., Vuik, C., 2022c. Hybrid-dimensional modeling for fluid flow in heterogeneous porous media using dual fracture-pore model with flux interaction of fracture-cavity network. J. Nat. Gas Sci. Eng. 104450. http://dx.doi.org/10.1016/j.jngse.2022.104450.

Wang, L., Golfier, F., Tinet, A.J., Chen, W., Vuik, C., 2022a. An efficient adaptive implicit scheme with equivalent continuum approach for two-phase flow in fractured vuggy porous media. Adv. Water Resour. 163, 104186. http://dx.doi.org/10.1016/j.advwatres.2022.104186.

Wang, Y., Shahvali, M., 2016. Discrete fracture modeling using centroidal voronoi grid for simulation of shale gas plays with coupled nonlinear physics. Fuel 163, 65–73. http://dx.doi.org/10.1016/j.fuel.2015.09.038.

Wang, Y., Vuik, C., Hajibeygi, H., 2022. Co2 storage in deep saline aquifers: impacts of fractures on hydrodynamic trapping. Int. J. Greenh. Gas Control 113, 103552. http://dx.doi.org/10.1016/j.ijggc.2021.103552.

Wang, L., Vuik, C., Hajibeygi, H., 2022b. A stabilized mixed-FE scheme for frictional contact and shear failure analyses in deformable fractured media. Eng. Fract. Mech. 267, 108427. http://dx.doi.org/10.1016/j.engfracmech.2022.108427.

Wesseling, P., 2001. Principles of Computational Fluid Dynamics. Springer-Verlag Berlin Heidelberg.

Wu, Y., Cheng, L., Killough, J., Huang, S., Fang, S., Jia, P., Cao, R., Xue, Y., 2021. Integrated characterization of the fracture network in fractured shale gas reservoirs—Stochastic fracture modeling, simulation and assisted history matching. J. Pet. Sci. Eng. 205, 108886. http://dx.doi.org/10.1016/j.petrol.2021.108886.

Yan, C., Jiao, Y.Y., Zheng, H., 2018. A fully coupled three-dimensional hydro-mechanical finite discrete element approach with real porous seepage for simulating 3D hydraulic fracturing. Comput. Geotech. 96, 73–89. http://dx.doi.org/10.1016/j.compgeo.2017.10.008.

Yin, T., Chen, Q., 2020. Simulation-based investigation on the accuracy of discrete fracture network (DFN) representation. Comput. Geotech. 121, 103487. http://dx.doi.org/10.1016/j.compgeo.2020.103487.

Zidane, A., Firoozabadi, A., 2018. Reservoir simulation of fractured media in compressible single-phase flow in 2D, 2.5D and 3D unstructured gridding. Adv. Water Resour. 121, 68–96. http://dx.doi.org/10.1016/j.advwatres.2018.08.005.

Zienkiewicz, O., Taylor, R., Zhu, J.Z., 2013. The Finite Element Method: Its Basis and Fundamentals, (seventh ed.) Elsevier, http://dx.doi.org/10.1016/C2009-0-24909-9.